Drop by drop backscattered signal of a 50x50x50m3 volume: A numerical experiment

Auguste Gires, Ioulia Tchiguirinskaia, D Schertzer

Drop by drop backscattered signal of a 50 x 50 x 50 m^3 volume: a numerical experiment

A. Gires[1], I. Tchinguirinskaia[1], and D. Schertzer[1]

(1) Université Paris-Est, Ecole des Ponts ParisTech, HM&Co, Marne-la-Vallée, France

Correspondence to: A. Gires (auguste.gires@enpc.fr)

Abstract

The goal of this paper is to analyse the influence of individual drop positions on backscattered radar signal. This is achieved through a numerical experiment: a 3D rain drop field generator is developed and implemented over a volume of 50 x 50 x 50 m^3, and then the sum of the electromagnetic waves backscattered by its hydrometeors is computed. Finally the temporal evolution over 1 second is modelled with simplistic assumptions. For the rainfall generator, the Liquid Water Content (LWC) distribution is represented with the help of a multiplicative cascade down to 0.5 m, below which it is considered as homogeneous. Within each 0.5 x 0.5 x 0.5 m^3 patch, liquid water is distributed into drops, located randomly uniformly according to a pre-defined Drop Size Distribution (DSD). Such configuration is compared with the one consisting of the same drops being uniformly distributed over the entire 50 x 50 x 50 m^3 volume.

Due to the fact that the radar wave length is much smaller than the size of a rainfall “patch”, it appears that, in agreement with the theory, we retrieve an exponential distribution for potential measures on horizontal reflectivity. Much thinner dispersion is noticed for differential reflectivity. We show that a simple ballistic assumption for drop velocities does not enable to reproduce radar observations, and turbulence should be taken into account. Finally the sensitivity of these outputs to the various model parameters is quantified.

Keywords:

Radar, raindrop, interference, scattering

1) Introduction

Weather radars are the only sensors capable of performing a spatio-temporal measurement of rainfall fields. It is a remote technique which basically relies on the analysis of the electro-magnetic field backscattered by hydrometeors in the atmosphere. It means that the quantity measured by radars is an electric field (or two electric fields when double polarizations are used), instead of the quantity hydro-meteorologists are interested in, like rain rate (or a Liquid Water Content, *LWC*). Weather radars suffer from numerous limitations which are due either to meteorological issues (natural vertical profiles of reflectivity, rainfall changes between the place of measurement and ground level,) or to the propagation of an electromagnetic wave in the atmosphere (beam blockage, attenuation, ground echo, anomalous propagation…) (Bringi and Chandrasekar 2001, Steiner 2005). In this paper we address the specific issue of how the micro-configuration of drops in position and size affects the large scale scattering properties. Indeed the electric field measured by radars is the sum of the ones backscattered by individual drops and can therefore be affected by constructive or destructive interferences leading to biased rain rate estimates. The study in this paper is focused on the backscattering by hydrometeors that is a first step towards improved radar measurement.

This issue is usually neglected by authors who simply assume a homogenous distribution of drops within the scanned volume (see Lawson and Uhlenbeck, 1950, for a first description of this statistical model). Some nevertheless addressed it. For example Jameson and Kostinski (2010a) analysed the time series of a given range bin with the help of spectral analysis and found evidence for coherent backscattering. In a refinement of this study, in which they also analysed the correlations between consecutive radar bins, they confirmed that observations could not be explained only by noise and associated them with the presence of structures in the rainfall fields being in resonance with the radar wavelength (Jameson and Kostinski, 2010b). They also noticed that this effect was much more pronounced with snow than with rainfall and that it increased with radar wavelength (no coherency would be observed if the radar wavelength tended to 0 mm). Erkelens et al. (2001) explained that many radar observations can be explained by incoherent hydrometeor scattering and coherent air scattering (known as Bragg scattering) due to the turbulent fluctuations of the refractive index. They derived a theoretical expression for coherent scattering by considering the influence of hydrometeors on the variations of refractive index. The importance of this effect increases with radar wavelength. Using dual frequency radar measurements and the fact that the two effects do not have the same dependency on radar wavelength they re-interpreted the cloud measurements data from Knight and Miller (1998). The effect of the refractive index is

not addressed here. Lovejoy et al. (1996) and Schertzer et al. (2012) adopted a different approach. They modelled sub-radar pixel variability with the help of Universal Multifractal (Schertzer and Lovejoy 1987, 2011) and derived a theoretical expression linking the actual radar reflectivity to the theoretical one obtained for incoherent scattering. The underlying idea being that the clustering of drops will lead to constructive interference.

In this paper we adopt an approach different than those previously mentioned, by setting up a purely numerical experiment to mimic backscattering by hydrometeors located within a volume of 50 x 50 x 50 m^3. In order to actually mimic radar measurements, other effects, such as antenna direction and range patterns, attenuation, propagation effect, or presence of non clear air along the path the radar wave, would have to be modelled. Some authors, for example, Capsoni and d'Amico (1998) and later Capsoni et al. (2001) for an extension to polarimetric quantities, developed radar simulators, but they did not take into account all the drops due to computation limitations (they used compressed Drop Size Distribution) and also assumed an homogenous distribution of drops within a radar bin. This was also the case for Cheong et al. (2008) who used an even smaller amount of hydrometeors per radar bin (few tens) but simulated time series. Here the contribution of all drops is taken into account, including their inhomogeneous distribution in space. Other radar simulators were developed to improve radar rainfall measurements (Anagnostou and Krajewki 1997 or Krajewski et al. 1993 for an earlier version; Doviak and Zrnic 1993) or to produce reflectivity maps from numerical weather models as a first step toward radar assimilation (Caumont et al. 2006). These radar simulators rely on the computation of integrals over radar bins and assume a homogenous distribution of drops, and no coherence effect. Radar data has also been used to calibrate a 4 level Poisson clustering process to model rainfall fields (Kavvas and Chen, 1989). More recently, this approach of numerical experiment has for example been used in Merker et al. 2015 to improve radar calibration, but not at the drop scale as done in this paper.

In order to achieve our goal of mimicking the scattering of hydrometeors contained within a 50 x 50 x 50 m^3 box we first develop a 3D rain drop field generator (section 2). Then we compute the electric field measured by the radar as the sum of the electric fields backscattered by each individual drops and test the influence of the drops' positions (section 3 on methodology). Finally results for single pulse measurements and successive ones over 1 s are discussed in section 4.

2) A large (few tens of meters) scale 3D drop simulator

The purpose of this paper is to mimic the scattering of a fixed volume by computing the electric field backscattered individually by all the hydrometeors it contains. The main challenge is to generate 3+1 D (3 dimensions in space and 1 dimension in time) rain drop fields. We aim at simulating during 1 s the signal backscattered by a fixed cubic (i.e. neither the shape nor the volume of an actual radar bin) volume of size 50 x 50 x 50 m^3.

In order to achieve this, we mainly rely of the findings of Lilley et al. (2006) who analysed the output of the HYDROP experiment (Desauliner-Soucy et al, 2001) consisting in the reconstruction of rain drop fields with most of the drops in a 8 m^3 volume with the help of stereo-photography; and Gires et al. (2015) who reconstructed vertical 35 m high columns above a 2D – Video Disdrometer. Their main conclusion was that rain drop related fields (number, LWC, …) basically exhibited a scaling behaviour well characterized with the help of Universal Multifractals (see Schertzer and Lovejoy 2011 for a recent review) down to 0.5 m. Below this scale a homogeneous distribution is found. Based on this a three step process is designed to generate a 3D rain drop field (see Fig. 1 for an illustration):

(i) An average *LWC* is set for the whole 50 x 50 x 50 m^3 volume (it is an input of the model) and a 3D conservative discrete Universal Multifractal (UM) cascade is implemented to distribute it over patches of size 0.5 x 0.5 x 0.5 m^3. Potential anisotropy between horizontal and vertical directions is not taken into account in this process. Such multiplicative cascade process is characterized with the help of only two parameters; C_1 the mean intermittency which quantifies the clustering of the average field (C_1 = 0 for a homogeneous fields), and α the multifractality index ($0 \le \alpha \le 2$) which quantifies how this mean intermittency evolves when considering field values slightly different from the average one. The greater the values of UM parameters C_1 and α, the stronger the extremes. Since the average value of the field is kept constant, the disparities between the patches will be more pronounced for greater values of UM parameters. C_1 and α are inputs of the model.

(ii) The second step consists in converting the liquid water within each patch (simply equal to the LWC_{patch} in $g.m^{-3}$ obtained at the end of the cascade process multiplied by 0.5 x 0.5 x 0.5 m^3) into drops. To achieve this, a discrete Drop Size Distribution is used $Nb(D_i)$ (the number of drops of diameter within the class D_i per unit volume). $Nb(D_i)$ is decomposed into two parts:

$$Nb(D_i) = N_t f(D_i) \quad (1)$$

Where N_t is the number per unit volume and $f(D_i)$ is simply the proportion of drops within a given class ($\sum_{class} f(Di) = 1$). $f(Di)$ is an input of the model. For each patch only $N_{t,patch}$ has to be evaluated. Finally the number of drops of a given class within a given patch is equal to $N_{t,patch} f(D_i)$. In practice the nearest integer is used. $N_{t,patch}$ is obtained by ensuring that the sum of the mass of all the drops equals the liquid water content of the patch:

$$LWC_{patch} V_{patch} = \rho_{wat} \frac{4}{3} \frac{1}{10^9} \pi N_{t,patch} \sum_i \left(\frac{D_i}{2} \right)^3 f(D_i) \quad (2)$$

With D_i in mm, ρ_{wat} the water volumic mass in g.m^{-3}, V_{patch} in m^3 and LWC_{patch} in g.m^{-3} and D_i in mm.

(iii) The last step consists in affecting a position to the drop centre. It is done with a simple random uniform law for all three directions within the patch.

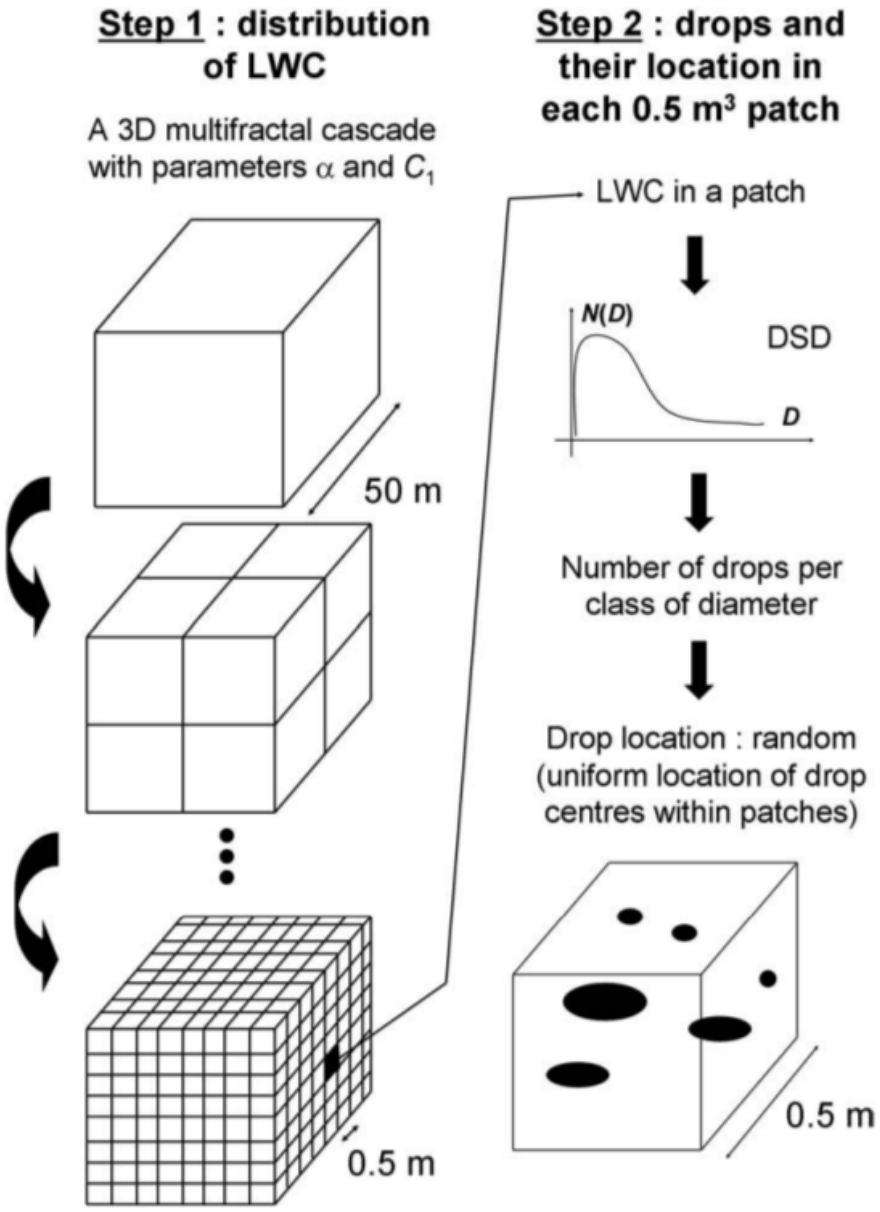

Figure 1. Illustration of the process designed to generate synthetic 3D rain drop fields

In section 4.3, we need to consider the temporal evolution of the drops over 1 s, i.e. simulate their movement. To achieve this, the following steps are implemented: (i) a larger volume is modelled (100 m in height) (ii) a velocity $\underline{v}$ is affected to each drop and used to locate them over successive time steps. Two velocities are tested:

- A purely vertical (along the vertical axis, characterized by a unit vector $\underline{e}_z$) ballistic one $\underline{v}_{bal}$, where a terminal fall velocity depending on the equi-volume diameter is used. The relation of Lhermitte (1988) is used:

$$\underline{v}_{bal}(D) = v_{bal}\underline{e}_z = 9.25 * (1 - \exp(-68002D^2 - 488D))\underline{e}_z \quad (3)$$

Where v_{bal} is in m.s^{-1} and D in mm. This standard assumption for drop velocity is done here, although some recent works showed that there were some discrepancies between "theoretical" fall velocity and actual fall velocity in real condition due notably to the constantly alive collision - break-up – relaxation process (Montero-Martinez et al. 2009). Deviations seem to be more pronounced for convective storms than stratiform ones (Niu et al. 2010, Thurai et al. 2013). It would be interesting to investigate the effect of this issue on radar measurement with a numerical simulator in future work.

- A turbulent one $\underline{v}_{turb}$, which takes into account a potential horizontal variability

$$\underline{v}_{turb} = v_{bal}\underline{e}_z + v_{trub,\max}(U\underline{e}_x + V\underline{e}_y) \quad (4)$$

where U and V are i.i.d. uniform random variables between -0.5 and 0.5. $v_{trub,\max}$ is a parameter set by the user defining the range of values over which the turbulent velocity can vary. Values equal to 1, 2, and 4 m.s^{-1} were tested. Adding a constant horizontal average wind for all drops did not affect the results that will be discussed in section 4.3, hence it is not done. The most relevant point is the differences of velocities between drops. The authors are aware that this is a very simplistic model that should be refined for further quantitative analysis but is sufficient for the illustrative purpose of this section.

Multifractal analysis were first carried out on the simulated LWC fields and then on the reconstructed (simply adding the contribution of each drop) LWC fields obtained after a 1s movement by a turbulent velocity to check whether the scaling properties of spatial clustering are preserved. Obviously input UM parameters are retrieved at the beginning of the process. For the reconstructed fields, the quality of the scaling decreases and UM parameters are slightly altered (a decrease for both is noted, more pronounced for C_1 and larger initial values), but the overall properties are kept.

3) Methods

Radars basically measure the intensity of the electric field backscattered by the hydrometeors located within the scanned volume. More precisely let us consider a radar located at (-r,0,0) in a Cartesian coordinate system that transmits a horizontally polarized wave E_h^{inc} with a wave length λ. See Fig. 2 for an illustration of the simulated configuration. The distance r between the radar transmitting the wave and the fixed volume whose backscattering is computed was

set to 15 km in this paper. A wave length equal to 33.3 mm corresponding to X-band is used in this paper and similar results are found for C and S band. The electric field $E_{h,drop}^{sca}$ backscattered by a drop located at the position (*x*,*y*,*z*) is equal to:

$$E_{h,drop}^{sca} \approx S_{hh,drop} e^{-i\phi_{tot,drop}} \quad (5)$$

Where:

- ≈ indicates proportionality; pre-factors, being considered as identical for all the drops located within the scanned volume, are neglected in this study. It means that all propagation effects (attenuation and phase shift of the horizontal and vertical components) along the path between the radar and the fixed volume containing the scattering hydrometeors are not addressed in this paper. Future works will include them, notably to take into account the variabilty of LWC at small spatio-temporal scales. Note that weighting functions to model antenna and pulse beamwidth are not used in this paper which focuses on the scattering by hydrometeors. Eq. 5 means that only mono-scattering is considered in this study (the order of magnitude of the maximum drop concentration is 10^3 m^{-3} here), and potential effects of multiple scattering, which tend to increase radar reflectivty (Kobayashi et al. 2005, 2007a, 2007b), are not taken into account.

- ϕ_{tot} is the total phase shift due the two way path between the radar and the drop. We have

$$\phi_{tot} = \frac{2\pi\delta}{\lambda} \quad (6)$$

With

$$\delta = 2\sqrt{(x+r)^2 + y^2 + z^2} \quad (7)$$

being the optical path

- S_{hh} is the complex scattering coefficient, computed for an angle corresponding to backscattering. This complex number was estimated for each scatterer (a drop) using the Python PyTMatrix library (Leinonen 2014) which relies on the T-Matrix code by Mishchenko et al. (1996). In order to carry out the computations, the following assumptions were made: (i) Oblate spheroids are used to model drop shapes. The axis ratio is determined from the drop's volume (through its equivolume sphere diameter) with the help of the relation described in Battaglia et al. 2010. Neither the flattening of drops at the bottom, nor their oscillations (Thurai et al. 2005, 2009, Okamura 2010) are taken into account. Additional details on the

computation of scattering properties of rain drops can be found in the recent review by Okamura and Oguchi (2010) and references therein. (ii) The unknown orientation of the drops, which is modelled through the canting angle between the symmetry axis along the short direction of the drop and the local zenith (Oguchi 1977, Okamura and Oguchi 2010), is taken into account by considering a value of S_{hh} averaged over a distribution of canting angles. The one used here is the same as in Leinonen (2012); i.e. a normal distribution with mean and standard deviation respectively equal to 0° and 7°, in agreement with the findings of Bringi et al. 2008 on artificial rain measurement. Experiments with a video precipitation sensor showed that the distribution in actual rainfall condition could be wider (mean and standard deviation respectively equal to 2.1° and 11°), and attributed these discrepancies to the wind (Liu et al. 2014). (iii) Computations are carried out at a temperature of 20°C (the complex refractive index of water is then equal to 8.208+1.886i).

The electric field measured by the radar is computed as the sum of the ones backscattered by each drop (typically few hundred millions in our simulations):

$$E_{h,radar} = \sum_{drops} E_{h,drop}^{sca} \approx \sum_{drops} S_{hh,drop} e^{-i\phi_{tot,drop}} \tag{8}$$

Which yields the observed intensity

$$I_{h,radar} = \left| E_{h,radar} \right|^2 \approx \left| \sum_{drops} S_{hh,drop} e^{-i\phi_{tot,drop}} \right|^2 \tag{9}$$

Finally this quantity is compared with the simple sum of the backscattering coefficients

$$I_{h,simple} \approx \sum_{drops} \left| S_{hh,drop} \right|^2 \tag{10}$$

which corresponds to what would be observed if there was no constructive (or destructive) interferences between the fields backscattered by each drop (homogeneous distribution of the drop centres).

Similar computations are carried out for the wave transmitted and received with a vertical polarization (replacing "*h*" by "*v*" in the notations), and the ratio between the intensities measured for both polarisations is estimated (a pseudo radar differential reflectivity):

$$I_{hv,radar} = \frac{I_{h,radar}}{I_{v,radar}} \tag{11}$$

In order to study the influence of constructive (or destructive) interferences due to the drops' locations, for each realisation of *LWC* 3D distribution, 100 realisations of drops' positions within its patch are generated. For each realisation the radar intensity at vertical and horizontal polarization is computed, leading to an ensemble of 100 samples for each radar quantity. The exceedance probability distribution, denoted *Pr*, is finally estimated by sorting the ensemble of values in increasing order and dividing the rank by the total number of samples. Finally, for each sample, another ensemble obtained by locating randomly homogeneously the same drops not only within its own patch but within the whole 50 x 50 x 50 m^3 volume is generated. An exceedance probability distribution is computed similarly for this second ensemble. This enables to study the potential effect of drop clustering (down only to the patch scale of 0.5 m) on the computed probability distribution.

The standard set of parameters used in this paper is $C_1 = 0.2$, $\alpha = 1.8$, $\langle LWC \rangle = 2$ g.m^{-3}, DSD type 1 (Fig. 3), elevation angle $\theta = 0°$ (Fig. 2). The sensitivity of the model to its various parameters is tested by successively varying only one of parameters, while keeping the others constant:

- Influence of UM parameters C_1 and α: C_1 equal to 0.05, 0.2, and 0.5; and α equal to 1.8, 1.2, and 0.6 is tested. This range of parameter values is somewhat typical among empirical estimates reported for the radar rainfall fields (e.g.,,Gires et al. 2011, Tchiguirinskaia et al, 2012, Verrier et al. 2010 and 2011). However, it remains larger than the one observed on 3D fields (Lilley et al. 2006; Gires et al. 2015) for which C_1 and α estimates are respectively in the lower and upper bound of the interval studied here. In this paper we keep the wider range of observed parameters to test in a more general way the influence of UM parameters.

- Influence of $\langle LWC \rangle$: $\langle LWC \rangle$ equal to 1, 2, 4, 7 g.m^{-3} is tested. This range of values is on the upper bound of standard observed ones (for example Leinonen et al. 2012 observed LWC in range 0.01-4 g.m^{-3}), because we wanted here to test extreme situations for which radar rainfall estimates are more sensitive.

- Influence of DSD type: two DSDs are tested and the normalized histograms according to the diameter class are displayed in Fig. 3. They correspond to the ones obtained with the help of a 2D-video disdrometer for two different minutes of an event studied in Gires et al. (2015). There are more drops with a larger diameter for the second type. It means that for a given

average LWC over the studied volume, there are more large drops for the DSD type 2. Both DSDs are likely to lack small drops given the low sensitivity of disdrometer measurements to small drops. However this should not be a significant issue given that backscattered intensity basically behaves as a power 6 of the diameter, which limits the influence of small drops. Although they are rather similar, the two DSDs yield significant differences in the backscattered signal. Hence it suggests that they are sufficiently different to illustrate the point that it is a crucial parameter that should be studied in more details in future work, including taking into account its spatial variability.

- Influence of the location of the scanned volume with regards to the radar: elevation angles θ equal to 0, 10, 20, 30, 40, 50, 60, 70, 80, 90° (for horizontally to vertically pointing radars) are tested. Fig. 2 illustrates the definition of θ.

For actual rainfall field the model parameters are not independent, and some correlations are noted (ex: between the *DSD* and the *LWC*). It means that if the purpose of the sensitivity analysis was to quantify measured uncertainties, there would have to be some correlation between the parameter changes to explore realistic ranges of possible values. In this first study we simply want to test their influence on the outputs, so they are modified independently from a standard situation.

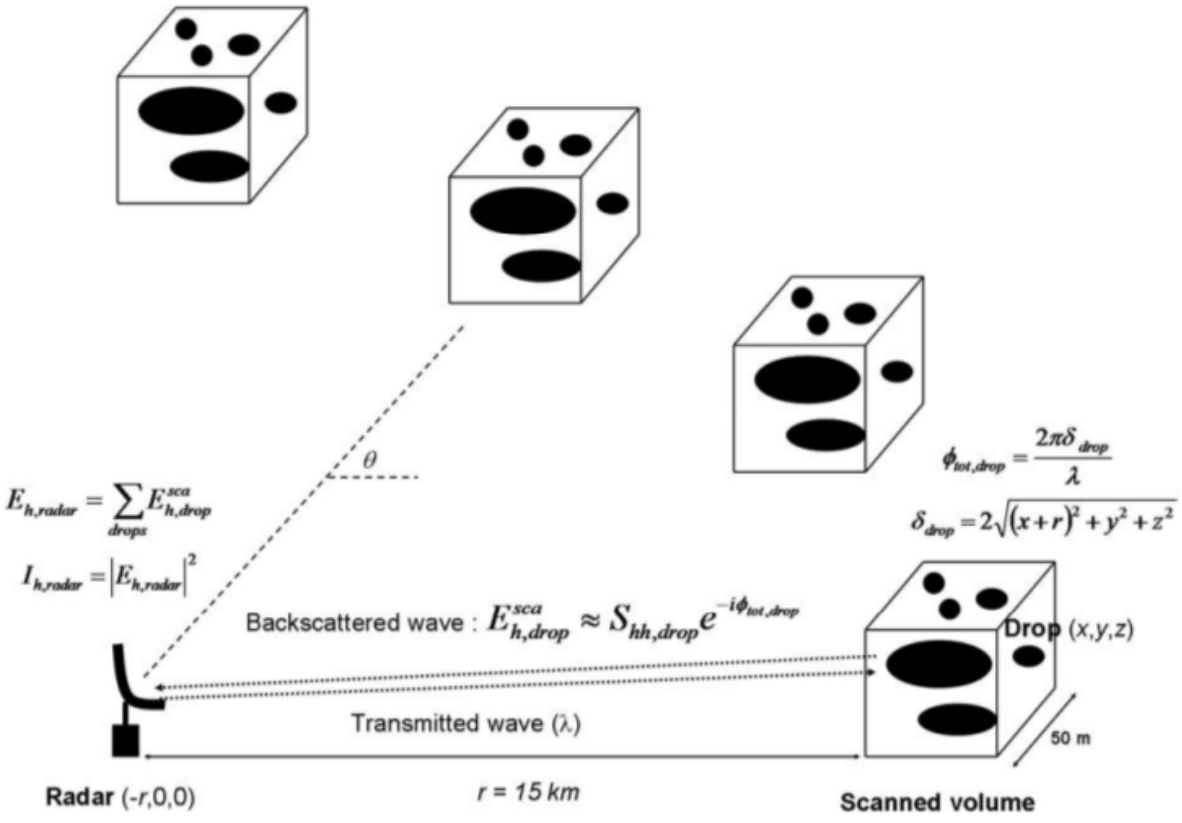

Figure 2. Illustration of the configuration tested for simulating radar observations of a 50 x 50 x 50 m^3 scanned volume.

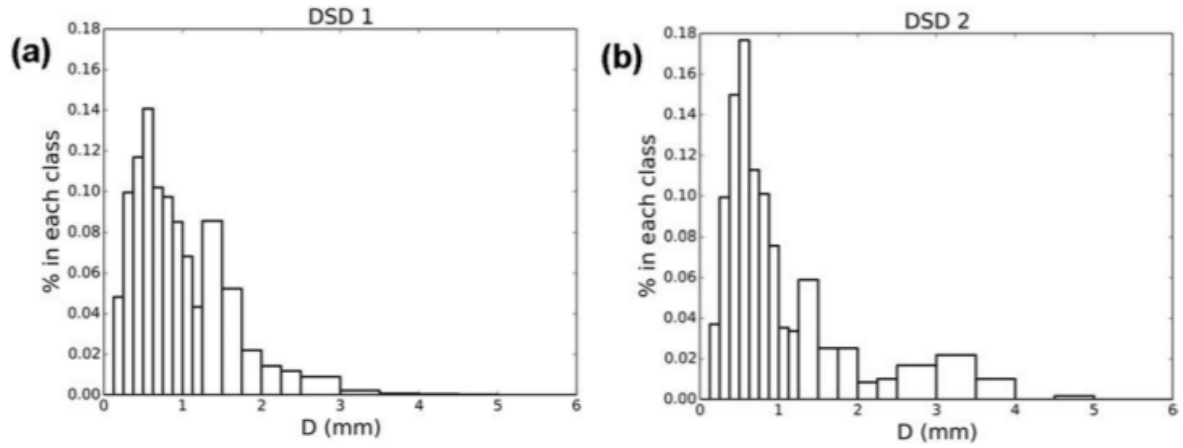

Figure 3. Histograms (% of drops according to class of diameters) for the two DSD types used in this paper.

4) Results and discussion

Before discussing the results, it should be mentioned that there is no data available at drop scale on such a large volume to properly validate the model developed here, which by the way is also the case for more homogeneous models commonly used in other works. Nevertheless it is in agreement with some prior results (based on imperfect data, Gires et al. 2015, Lilley et al. 2006) hinting at scaling properties down to 0.5 m. Further investigations involving both instrumentations and modelling developments will be needed to improve it as well as to validate it.

4.1) Horizontal reflectivity

In this section we only consider the backscattered intensity measured horizontally by a radar transmitting a horizontal wave. Figure 4.a displays the exceedance probability distribution for an ensemble obtained from a realisation of LWC 3D distribution with C_1 = 0.2, α = 1.8 ($<LWC>$ = 2 g.m^{-3}, DSD type 1, elevation angle θ = 0°). The curve corresponding to the drops' positions affected within their patch is in red whereas the one with the drops' positions affected within the whole volume is in blue. The green vertical line corresponds to the values obtained with the simple sum (Eq. 10), which is the same for all the samples given that the same drops with different locations are considered.

The first striking feature is that the two curves are very similar. It means that affecting the positions of the drops within a patch or within the whole volume does not change the range of explored values due the constructive or destructive interferences between the electric fields backscattered by each drop. In other words the clustering of drops does not yield additional constructive interferences. This finding is in apparent contradiction with the ones of Lovejoy et al. (1996) and Schertzer et al. (2012). It is actually simply due to the fact that in the specific model implemented here the clustering of drops stops at 0.5 m which is much greater than the radar wave length (few cm for radar wavelength), which was not the case in the previously mentioned paper. This decorrelation between drops and atmospheric turbulence, set here at 0.5 m, is likely to occur at much smaller scale in clouds where drops / droplets are actually smaller and therefore more sensitive to wind effects (see Lilley et al. 2006 and Gires et al. 2015 for a discussion on this point; or Schmitt et al. 1998 or de Montera et al, 2010 on the passive scalar like behaviour on rain drops and the coupling with turbulence), meaning that a different model should be used to study cloud radar observations (Erkelens et al., 2001). To clarify this point a closer look at Eq. 6 indicates that the influence of the drops' locations on the backscattered wave is limited to the decimal part of the ratio between the optical path and radar wave length $\frac{\delta}{\lambda}$ (the integer part does not need to be considered given that $e^{2i\pi N}=1$). If the patch size is much larger than λ, then this ratio will be homogeneously distributed and drop clustering does not affect the results. It also means that if some rainfall structures are in resonance with the radar wavelength then some constructive interferences could be observed. This effect is discussed in Jameson and Kostinski (2010), and not observed with the developed model.

The distribution of measured intensity according to the sample of drop locations is skewed and covers a wide range of possible values. It can be shown theoretically that if drop centres are homogeneously (uniformly) distributed, the distribution actually follows an exponential law. The proof, which relies on the central limit theorem, can be found in Lovejoy and Schertzer (1990). As a consequence one expects:

$$\Pr(I_{h,radar}\,|I_{h,simple}) = \frac{1}{I_{h,simple}} e^{-I_{h,radar}/I_{h,simple}} \qquad (12)$$

In order to confirm this $\log(\Pr)$ vs. $I_{h,radar}$ is plotted in Fig. 4.b for the same ensembles as in Fig. 4.a. The expected straight lines are retrieved. Linear regressions implemented on the

whole ensemble yield inverses of the slopes equal to 113730 and 112812 for respectively the ensemble with and without clustering (coefficient of determination greater than 0.98). These values are very similar and also close (7% or less) to both $I_{h,simple}$ (105688) and the mean of the ensemble (107583) to which they should be equal for an exponential distribution. Similar results are found for the other generated ensembles of this paper.

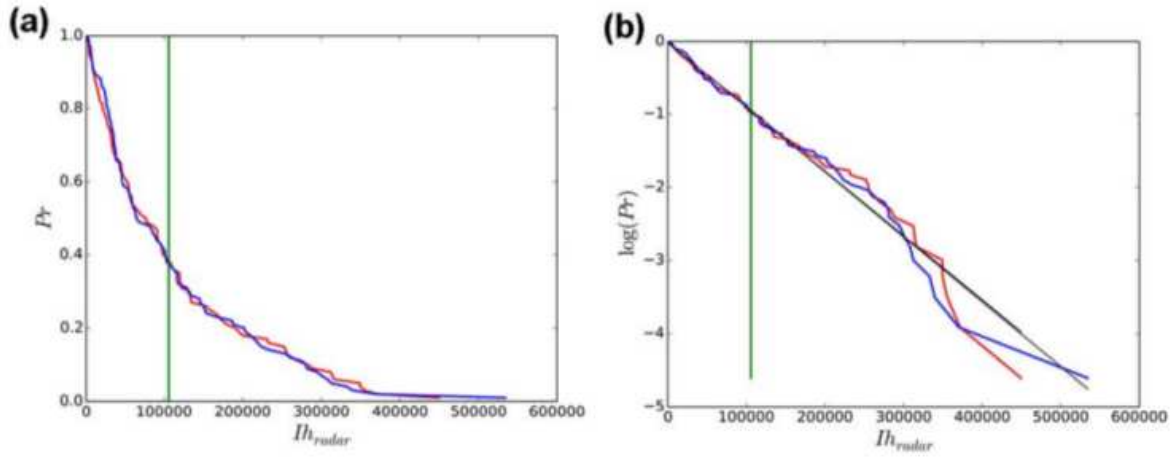

Figure 4. (a) Exceedance probability distribution Pr in the ensemble of radar observations $I_{h,radar}$ for a given *LWC* 3D distribution; (red) drops location with clustering down to 0.5 m. (blue) drop locations without clustering (b) Same as in (a) expect that log(Pr) is plotted instead of Pr.

Then the influence of the various parameters of the model is analysed, beginning with UM parameters. Figure 5.a and b (c and d) display respectively the exceedance probability (or its log) vs. the radar intensity for various values of C_1 (α), keeping all the others constant. As in Fig. 4 the red curves are obtained with clustering (down to 0.5 m) while the blue ones are obtained without clustering. Each curve is actually an average obtained with 3 ensembles of 100 samples obtained from a given *LWC* 3D distribution. This was done to highlight more clearly the differences found for the various UM parameters which were less visible than those for the other parameters. The same qualitative results, i.e. an exponential distribution of the possible values according to the drop position and no influence of the drop clustering (which stops at 0.5 m), are observed for all the parameter sets. Quantitatively it appears that the retrieved radar intensities increase with C_1. This effect is somehow an artefact of the

model. When C_1 increases the variability / extremes in the *LWC* 3D distribution is stronger, meaning the some patches will have much greater values since the average *LWC* remains constant. These greater values in some patches mean that more large drops will be located in it. Indeed when the liquid volume of each patch is converted into drops using the DSD, the nearest integer is used as the number of drops of a given class. It means that greater quantities of water enable to explore more the tail of the DSD, which corresponds to the drops backscattering more significantly radar waves. Histograms (not shown here) of drops per class confirm this interpretation. Given that the range of values for C_1 explored in the sensitivity analysis is wider than expected from available observations for rainfall (see section 3), this effect is likely to have less influence on actual measurements than noted here. No influence of α is observed.

Figure 5.e and f display the same curves as in Fig. 5.a and b but for varying average *LWC*. The only difference is that the curves obtained for each ensemble of 100 samples of drop positions for a given *LWC* 3D distribution are plotted individually and not on average. The results simply confirm expectations; i.e. same qualitative results as before and the retrieved radar intensity obviously increases with greater values of *LWC*. The curves associated with a given value of average *LWC* are clearly distinguishable from the ones for another value.

Figure 6.g and h are the same ones but for the two DSD types, with again the same qualitative results. Quantitatively as expected all parameters being constant the DSD with heavier tail (DSD 2) yields greater values of radar intensities since it basically depends on the drops' diameters to the power 6. Given the strength of this effect especially for DSD not so significantly different, it would be important to analyse in future works the influence of the strong hypothesis of homogeneous DSD over the scanned volume. Indeed spatial and temporal variations in DSD (Schleiss and Smith, 2015) could yield different results. This will be studied in future investigations.

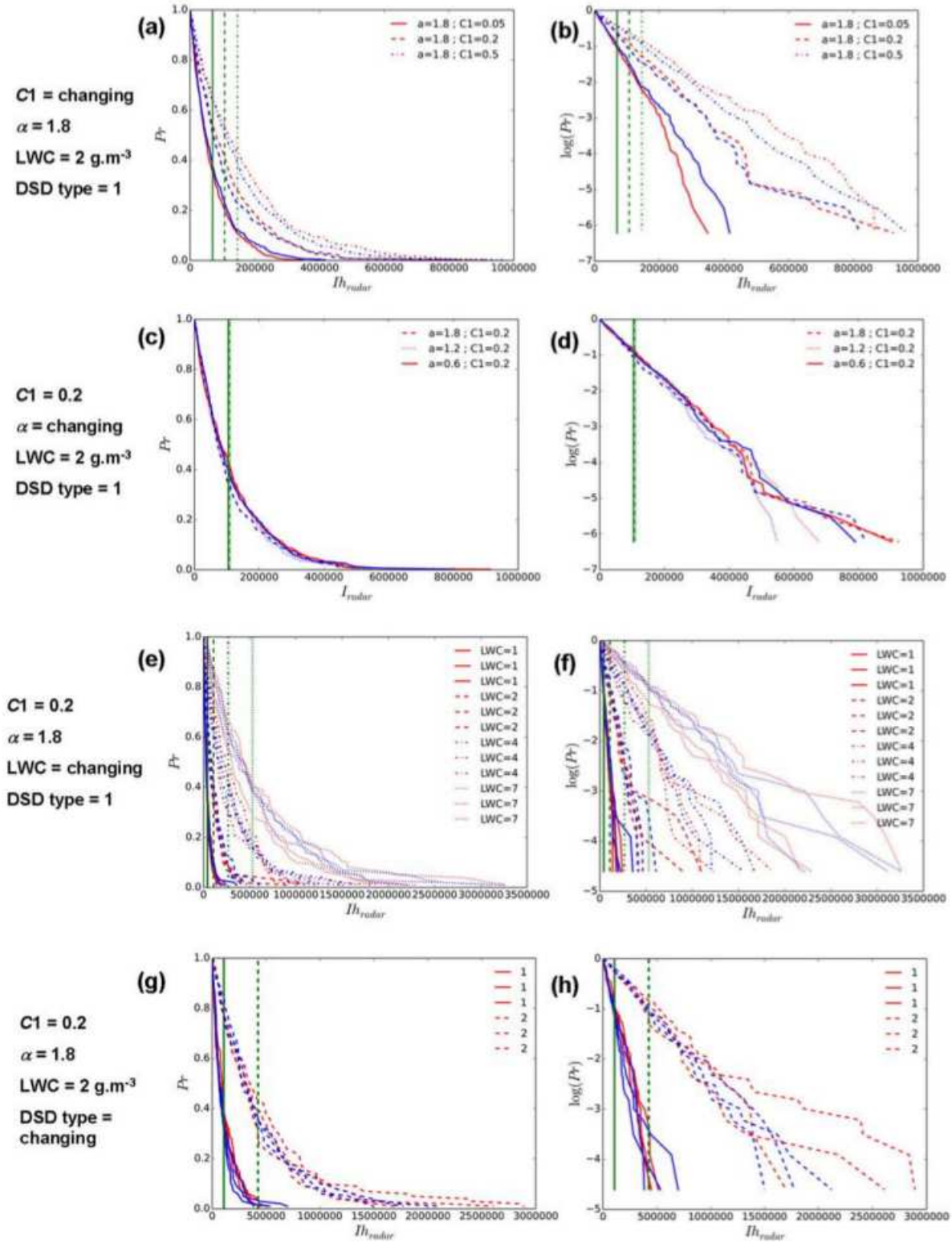

Figure 5. Influence of the various parameters of the model on the retrieved radar intensities. (left) Exceedance probability distribution Pr in the ensemble of radar observations $I_{h,radar}$ for a given *LWC* 3D distribution; (right) same as in (left) but plotting log(Pr) instead of Pr. (red) drops location with clustering down to 0.5 m. (blue) drop locations without clustering.

4.2) Differential reflectivity

In this section we analyse not only $I_{h,radar}$ but also $I_{v,radar}$ and $I_{hv,radar}$, the ratio between the two. We also consider elevation angles θ ranging from 0 to 90°. As commonly done in this paper, for a given parameter set, an ensemble of 100 samples corresponding to different drops' positions is generated (either considering clustering down to 0.5 m or not). Here the standard configuration is used, only θ varies. Figure 6.a and b. display the mean among the ensemble of values for respectively $I_{h,radar}$ and $I_{v,radar}$, when clustering is considered (very similar results are found without clustering), as a function of θ. As expected the differences between the intensity between the two polarizations is maximum for $\theta = 0°$ and null for $\theta = 90°$ (an oblate spheroid seen from below "looks like" a circle). The maximum ratio obtained between the two is equal to 1.5.

The relevant feature is visible in Figure 6.c which displays a pseudo coefficient of variation (*CV'*) within the ensemble for each angle. *CV'* is defined as the difference between the 90% and 10% quantile divided by twice the mean. It is expressed in %. This pseudo coefficient of variation is used rather than the standard one because the underlying probability distributions are skewed. It appears that *CV'* is very close for both $I_{h,radar}$ and $I_{v,radar}$, and tends to very slightly decrease with greater θ. The values are also much greater that the ones found for $I_{hv,radar}$ (140% vs. 25%), which means that the dispersion within the ensemble is much smaller for $I_{hv,radar}$. This quantity is therefore less sensitive to individual drop positions and its estimates more robust. This is due to the fact that the constructive (or destructive) interferences between the electric field backscattered at each polarization by drops are correlated; i.e. to simplify $I_{h,radar}$ and $I_{v,radar}$ are affected by the same kind of interferences.

In order to have a closer look at the obtained distributions, Fig. 7 displays the exceedance probability as a function of $I_{h,radar}$ (Fig. 7.a), $I_{v,radar}$ (Fig. 7.b) and $I_{hv,radar}$ (Fig. 7.c). They are the same curves as in Fig. 4 and 5 right columns. They are plotted for the two DSD types, with 3 ensembles for each DSD type (i.e. 3 realisations of *LWC* 3D distribution are tested). The behaviour observed for the vertical polarization output $I_{v,radar}$ is very similar to the one found for $I_{h,radar}$ which has been discussed in the previous section (exponential distribution,

simply with lower values, Fig. 7.b). On the contrary as hinted with the analysis of *CV'*, the distribution of $I_{hv,radar}$ exhibits a completely different shape with much less dispersion (Fig. 7.c). It is neither an exponential nor a Gaussian distribution.

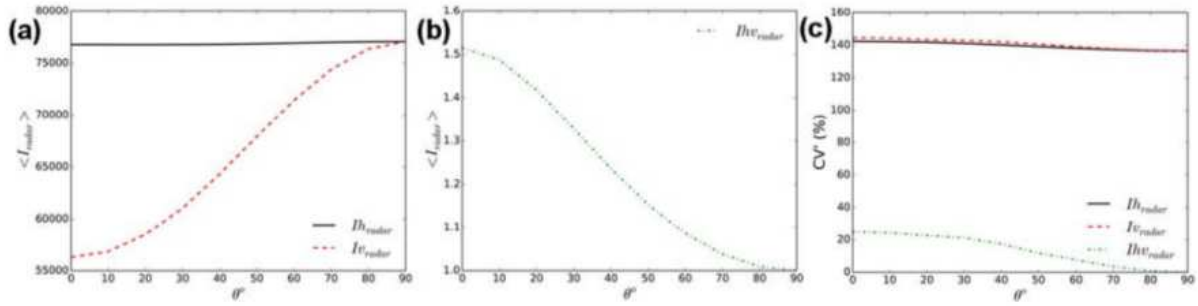

Figure 6. $\langle I_{h,radar} \rangle$ and $\langle I_{v,radar} \rangle$ (a) and $\langle I_{hv,radar} \rangle$ (b) as a function of the elevation angle θ. (c) *CV'* within each ensemble of simulated $I_{h,radar}$, $I_{v,radar}$ and $I_{hv,radar}$ as a function of the elevation angle θ.

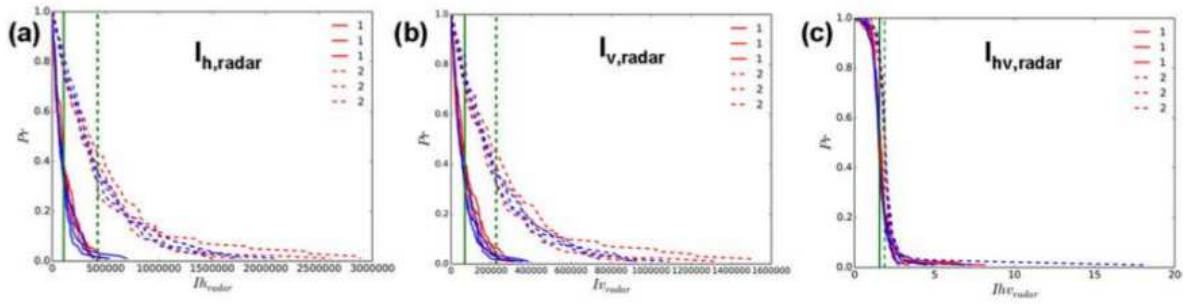

Figure 7. Exceedance probability distribution Pr in the ensemble of radar observations for $I_{h,radar}$ (a), $I_{v,radar}$ (b) and $I_{hv,radar}$ (c). For each DSD type (1 or 2), the results corresponding to three ensembles, each obtained for a realisation of *LWC* 3D distribution, are displayed.

4.3) Consequences on radar remote sensing

In this section the consequences of the previous findings in terms of remote sensing are explored, keeping in mind that only the scattering is taken into account in this paper, and no other radar issues. The first obvious one is that a single pulse is not enough to achieve a robust measure. Indeed as shown before a single measure basically yields any measured intensity over a wide range; and it is impossible to relate it to a given average *LWC* or rain rate. This is precisely why in practice; an average over typically 100 – 200 pulses over approximately 0.1s is used. The underlying assumption is that the successive pulses

correspond to independent realisations of the drop positions (drops are moving during this time interval), meaning that the average value over the pulses yields the desired quantity I_{simple}, which is free of possible interferences influence.

In order to study this issue, we use the model presented in section 2, with either a ballistic or a so called "turbulent" velocity affected to each drop, to represent the temporal evolution over 1 s. Figure 8 (left column) displays the temporal evolution of the backscattered intensity by the radar in the horizontal polarisation (standard set of parameters is used) for different values of $v_{trub,\max}$. Computations are carried out each 0.002 s (500 time steps for the simulated second). Similar curves were found for other realisations. The green long-dash curve corresponds to $I_{simple,bal}$ and is basically constant during the simulated second. The slight variation noticed on the curve is simply due to the fact that at each time step some drops are entering the studied volume from the top and some are leaving from the bottom. Given that it is not exactly the same ones, this results in slight variations of total water content. Here the slight decrease means that for this specific realisation, the *LWC* was slightly larger at the bottom than at the top of the generated volume. The curves obtained with the "ballistic" or "turbulent" velocities are plotted respectively in dash blue and solid red. Figure 8 (right column) displays the same curves but with an average over 0.1 s (moving window). It appears that the fluctuations observed at the highest temporal resolution quickly increase with the level of turbulence inputted in the model (simplistically represented with the help of $v_{trub,\max}$). With the 0.1 s moving window average; the slow fluctuations without turbulence (simply $\underline{v}_{bal}$) are not dampened. This can be considered as surprising given that during a 0.1 s interval drops are moving 5 to 80 cm in this case, which is greater than the radar wave length. It is due to the fact that the correlations between the drop velocities are too strong. This results in realisations of drops' locations that are not independent enough to validate the assumption that successive pulses yield independent realisations. Same kind of "slow" fluctuations are noted on other realisations, with usually large deviations (either positive or negative) from the I_{simple} curve. When the turbulent velocity $\underline{v}_{turb}$ is increased, it appears that fluctuations are much more pronounced at the highest temporal resolution, and 0.1 s average closer to the I_{simple} (more visible for $v_{trub,\max} = 4$ m.s^{-1}). This is more in agreement with radarist experience. To investigate further this point, the decorrelation time of the signal was computed for the

various values of $v_{trub,\max}$, similarly to what Capsoni et al. (2001) did. Results are plotted Fig. 9, and enable to quantify more precisely this effect. If a level of autocorrelation equal to 0.5 is taken as a threshold to define the decorrelation time, we find values equal to 200, 16, 9 and 5 ms for $v_{trub,\max}$ equal to respectively 0, 1, 2 and 4 m.s^{-1}. These values are compatible with Capsoni et al. (2001) findings. It means that to properly reproduce backscattering properties of the hydrometeors within the fixed volume, one has to take into account turbulent velocity of drops. Further investigations taking into account radar technology aspects (antenna and beam pattern…) will be needed to confirm this on radar measurement. It is likely that a more realistic model of turbulent velocities would yield better results.

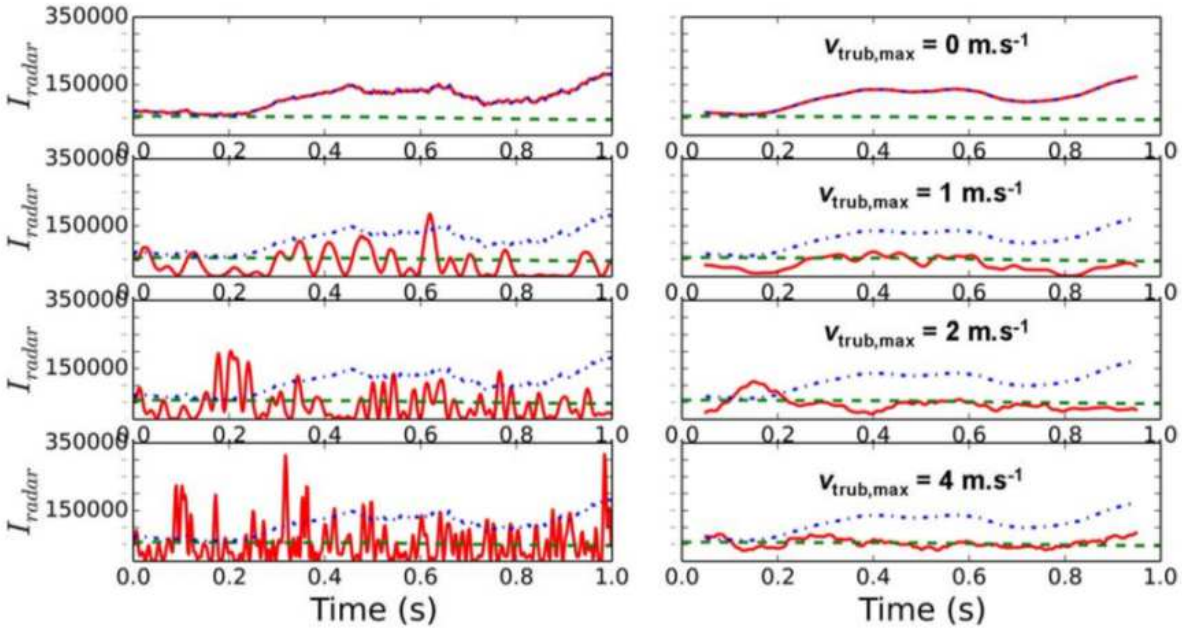

Figure 8. (Left columns) Temporal evolution of the intensity measured by a radar on the horizontal polarisation ($I_{h,radar}$) during 1 s, by modelling drops either with a "ballistic" (dash blue) or "turbulent" (solid red) velocity, along I_{simple} (long dash green). Each line correspond to a value of $v_{turb,\max}$ (Right column) Same as in left, with a 0.1 s moving window average.

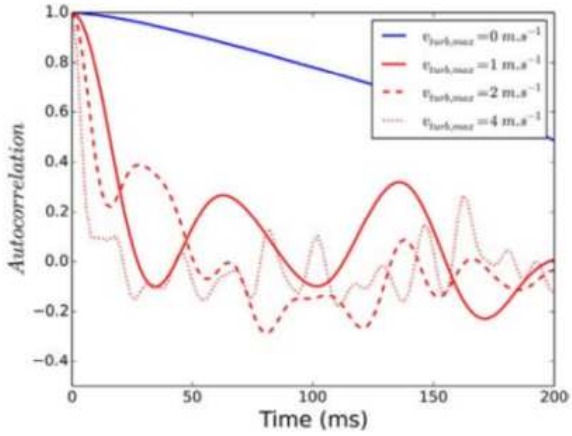

Figure 9. Autocorrelation of the simulated backscattered signal for various values of $v_{turb,\max}$.

5) Conclusions

In this paper, we developed a 3D rain drop field generator. We used it to numerically mimic the scattering produced by hydrometeors contained in a fixed scanned volume of 50 x 50 x 50 m^3 and its evolution over 1 s. The model is based on Universal Multifractal cascades down to 0.5 m and a homogeneous distribution of drops below.

The primary goal was to investigate the influence of drops' positions, and we show that as theoretically expected, we retrieve an exponential distribution for potential measured horizontal reflectivity. Given that 0.5 m is much greater than the radar wavelength, we found that the clustering of drops has no influence on the results. The model was developed for rain drops, and it should be revisited to adapt it to cloud droplets. Indeed they are much smaller and therefore more likely to remain correlated to wind turbulence and behave as a passive scalar down to scales smaller than 0.5 m and possibly smaller than the radar wavelength. Interestingly, a much thinner dispersion of values according to drops' positions is observed on differential reflectivity due the correlation between the interferences associated to horizontally and vertically polarized waves. Now that the 3D rain drop field generator is available, it should be used in future works to develop an actual radar simulator taking into account effects such as antenna direction and range weighting functions, or propagation effect between the radar and hydrometeors (notably the presence of non clear air), on a more representative geometrical setting (not a cubic box). This would enable to actually investigate the influence

of drops' positions on the various parameters of the rainfall estimation process with radars. Other radar quantities, such as the attenuation, the (specific) differential phase and the standard radar relations linking them to rain rates, should also be addressed in extended version of this model. A crucial point will also be to study more precisely the role of the DSD, which has been shown to be one of the most influential inputs of the model, and notably to relax the coarse assumption of a homogenous DSD over the scanned volume, as argued in this paper.

The analysis of the temporal evolution over 1 s showed that a simple ballistic velocity for drops did not enable to reproduce radar measurements, and that a "turbulent" velocity should be introduced. Currently a very simplistic model was implemented and further investigation should include a coupling with a much more realistic model of wind turbulence, for example one simulated with multifractal cascades (Schertzer and Tchiguirinskaia, 2015), to reproduce more accurately radar measurements.

Finally, it will be necessary to confront this numerical experiment with dedicated scans of actual radar measurements. This will be possible with the newly operating X-band radar installed on the campus of Ecole des Ponts ParisTech where the authors are working.

Acknowledgements

The authors thank Alexis Berne for fruitful discussion and suggestions in the framework of Partenariat Hubert Curien – Germaine de Staël (PROJET N° 32709UK). The authors greatly acknowledge partial financial support form the Chair "Hydrology for Resilient Cities" (endowed by Veolia) of Ecole des Ponts ParisTech, and EU NEW-INTERREG IV RainGain Project (www.raingain.eu).

References

Anagnostou , E.N., Krajewski, W. F., 1997. Simulation of radar reflectivity fields : Algorithm formulation and evaluation. Water Resources Research 33(6), 1419-1428.

Battaglia, A., Rustemeier, E., Tokay, A., Blahak, U., Simmer, C., 2010. PARSIVEL Snow Observations: A Critical Assessment. Journal of Atmospheric and Oceanic Technology 27(2), 333-344.

Beard, K.V., 1977. Terminal velocity adjustment for cloud and precipitation aloft. J. Atmos. Sci. 34, 1293-1298.

Bringi, V. N., Chandrasekar, V., 2001. Polarimetric Doppler weather radar: principles and applications. Cambridge University Press, New York, USA.

Bringi, V.N., Thurai, M., Brunkow, D.A., 2008. Measurements and inferences of raindrop canting angles. Electronics Letters 44(24), 1425-1426.

Capsoni, C., D'Amico, M., 1998. A physically Based Radar simulation. Journal of Atmospheric and Oceanic Technology 15(2), 593-598.

Capsoni C. , D'Amico, M., Nebuloni, R., 2001. A Multiparameter Polarimetric Radar Simulator. Journal of Atmospheric and Oceanic Technology 18(11), 1799-1809.

Caumont O. et al., 2006. A Radar Simulator for High-Resolution Nonhydrostatic Models. Journal of Atmospheric and Oceanic Technology 23(8), 1049-1067.

Cheong, B.L., Palmer, R.D., Xue, M., 2008. A times series weather radar simulator based on high resolution atmospheric model. Journal of Atmospheric and Oceanic Technology 25(2),230-243.

De Montera, L., Verrier, S., Mallet, C., Barthes, L., 2010. A passive scalar-like model for rain applicable up to storm scale, Atm. Res. 98(1), 140-147.

Desaulnier-Soucy, N., Lovejoy, S., Schertzer, D., 2001. The continuum limit in rain and the HYDROP experiment. J. Atm. Res. 59-60, 163-197.

Doviak R. J. and D. S. Zrnic 1993 :Doppler Radar and weather observations 2nd ed. academic Press 562 pp.

Erkelens, J. S., Venema, V. K. C., Russchenberg, H. W. J., Ligthart, L. P., 2001. Coherent scattering of microwaves by particles: evidence from clouds and smoke. J. Atmos. Sci. 58, 1091–1102, doi: http://dx.doi.org/10.1175/1520-0469(2001)058<1091:CSOMBP>2.0.CO;2.

Gires, A., Tchiguirinskaia, I., Schertzer, D., Lovejoy, S., 2011. Analyses multifractales et spatio-temporelles des précipitations du modèle Méso-NH et des données radar. Hydrol. Sci. J. 56(3), 380-396

Gires, A., Tchiguirinskaia, I., Schertzer, D., Berne A., 2015. 2DVD Data Revisited: Multifractal Insights into Cuts of the Spatiotemporal Rainfall Process. Journal of Hydrometeorology 16(2), 548-562, doi: 10.1175/JHM-D-14-0127.1.

Jameson, A., Kostinski, B., 2010a. Partially coherent backscatter in radar observations of precipitation. J. Atmos. Sci. 67, 1928–1946, doi: http://dx.doi.org/10.1175/2010JAS3336.1.

Jameson, A., Kostinski, B., 2010b. Direct observations of coherent backscatter of radar waves in precipitation. J. Atmos. Sci. 67, 3000–3005, doi: http://dx.doi.org/10.1175/2010JAS3488.1.

Kawas, M. L., Chen Z., 1989. A radar-based stochastic model for the time-space arrivals of the rain fields onto a geographical region. Stochastic Hydrology and Hydraulics 3(4) , 261-280.

Knight, C., Miller, L., 1998. Early radar echoes from small, warm cumulus: bragg and hydrometeor scattering. J. Atmos. Sci. 55, 2974–2992, doi: http://dx.doi.org/10.1175/1520-0469(1998)055<2974:EREFSW>2.0.CO;2.

Krajewski, W., Raghavan, R., Chandrasekar, V., 1993. Physically based simulation of radar rainfall radar using a space time rainfall model. Journal of Applied Meteorology and Climatology 32 (2), 268-283.

Kobayashi, S., Oguchi, T., 2007a. Multiple-scattering formulation of pulsed beam waves in hydrometeors and its application to millimeter-wave weather radar. IEEE Geosci. Remote Sens. Lett. 4, 13-17.

Kobayashi, S., Ito, S., Tanelli, S., Oguchi, T., Im, E., 2007b. A time-dependent multiple scattering theory for a pulsed radar with a finite beamwidth. Radio Sci. 42, RS4001, doi:10.1029/2006RS003555.

Kobayashi, S., Tanelli S., Im E., 2005. Second-order multiple scattering theory associated with backscattering enhancement for a millimeter wavelength weather radar with a finite beam width. Radio Sci. 40, RS6015, doi:10.1029/2004RS003219.

Kobayashi, S., Oguchi, T., Tanelli, S., Im, E., 2007. Backscattering enhancement on spheroid-shaped hydrometeors: Considerations in water and ice particles of uniform size and Marshall-Palmer distributed rains. Radio Sci. 42, RS2001, doi:10.1029/2006RS003503.

Lawson, J. L., Uhlenbeck, G. E., 1950. Threshold Signals. McGraw-Hill, New York, USA.

Leinonen, J., 2014. High-level interface to T-matrix scattering calculations: architecture, capabilities and limitations. Optics Express 22(2), 1655-1660.

Leinonen, J., Moisseev, D., Leskinen, M., Petersen, W.A., 2012. A Climatology of Disdrometer Measurements of Rainfall in Finland over Five Years with Implications for Global Radar Observations. Journal of Applied Meteorology and Climatology 51(2), 392-404.

Lhermitte, R., 1988. Cloud and precipitation sensing at 94 GHz. IEEE Trans. Geosci. Remote Sens. 26, 207–216.

Lilley, M., Lovejoy, S., Desaulniers-Soucy, N., Schertzer, D., 2006. Multifractal large number of drops limit in rain. J. Hydrol. 328(1-2), 20-37, 2006.

Liu, X.C., Gao, T.C., Liu, L., 2014. A video precipitation sensor for imaging and velocimetry of hydrometeors. Atmos. Meas. Tech. 7(7), 2037-2046, www.atmos-meas-tech.net/7/2037/2014/ doi:10.5194/amt-7-2037-2014

Lovejoy, S., Schertzer, D., 1990. Multifractals, universality classes, satellite and radar measurements of clouds and rain. J. Geophys. Res. 95, 2021-2034.

Lovejoy, S., Duncan, M.R., Schertzer, D., 1996. Scalar Multifractal Radar Observers Problem. J. Geophys. Res. 101, 26479-92.

Merker, C., Peters, G., Clemens, M., Lengfeld, K., Ament, F., 2015. A novel approach for absolute radar calibration: formulation and theoretical validation. Atmos. Meas. Tech. 8, 2521-2530, doi:10.5194/amt-8-2521-2015.

Mishchenko, M.I., Travis, L.D., Mackowski, D.W., 1996. T-matrix computations of light scattering by nonspherical particles: A review. Journal of Quantitative Spectroscopy and Radiative Transfer 55(5), 535-575.

Montero-Martinez, G., Kostinski, A., Shaw, R., Garcia-Garcia, F., 2009. Do all raindrops fall at terminal speed? Geophysical Research Letters 36, L11818, doi:10.1029/2008GL037111.

Niu, S., Jia, X., Sang, J., Lu, C., Liu, Y., 2010. Distributions of Raindrop Sizes and Fall Velocities in a Semiarid Plateau Climate: Convective versus Stratiform Rains. Journal of Applied Meteorology and Climatology 49(4), 632-645, doi: 10.1 I75/2009JAMC2208.1

Oguchi, T., 1977. Scattering properties of Pruppacher-and-Pitter form raindrops and cross polarization due to rain: Calculations at 11, 13, 19.3, and 34.8 GHz. Radio Sci. 12, 41-51.

Okamura, S., Oguchi, T., 2010. Electromagnetic wave propagation in rain and polarization effects. Proceedings of the Japan Academy. Series B, Physical and Biological Sciences 86(6), 539-562, http://doi.org/10.2183/pjab.86.539

Sachinanda, M., Zrnic D.S. 1987. Rain Rate Estimates from Differential Polarization Measurements. Journal of Atmospheric and Oceanic Technology, 4(4), 588-598.

Schertzer, D., Lovejoy, S., 2011. Multifractals, generalized scale invariance and complexity in geophysics. International Journal of Bifurcation and Chaos 21(12), 3417-3456.

Schertzer, D., Tchiguirinskaia, I., Lovejoy, S., 2012. Getting Higher Resolution Rainfall Estimates: X-Band Radar Technology and Multifractal Drop Distribution. Proceedings of the Weather Radar and Hydrology Symposium Held in Exeter, UK, April 2011, IAHS Publ. 351.

Schertzer, D., Tchiguirinskaia, I., 2015. Multifractal vector fields and stochastic Clifford algebra, Chaos, 25, 123127(1-17), doi: 10.1063/1.4937364.

Schleiss, M., Smith, j., 2015. A Method to Estimate the 3D–Time Structure of the Raindrop Size Distribution Using Radar and Disdrometer Data. J. Hydrometeor, 16, 1222–1242.

Schmitt, F., Schertzer ,D. L. , Lovejoy, S., Brunet, G., 1996. Mulfractal temperature and flux of temperature variance in fully developed turbulence. Europhys. Lett., 34(3), 195-200.

Steiner, M., 2005. Estimation of Precipitation Using Ground-based, Active Microwave Sensors. In Encyclopedia of hydrological sciences, Anderson M.G. (ed), Wiley.

Tchiguirinskaia, I., D. Schertzer, C. T. Hoang and S. Lovejoy, 2012: Multifractal study of three storms with different dynamics over the Paris region. *Weather Radar and Hydrology*. R. Moore, S.J. Cole and A.J. Illingworth Eds. IAHS Press Wallingford U.K., 421-426

Thurai, M., Bringi, V.N., 2005. Drop axis ratios from 2D video disdrometer. J. Atmos. Ocean. Technol. 22(7), 966-978.

Thurai, M., Szakáll, M., Bringi, V.N., Beard, K.V., Mitra, S.K., Borrmann, S., 2009. Drop shapes and axis ratio distributions: Comparison between 2D video disdrometer and wind-tunnel measurements. Journal of Atmospheric and Oceanic Technology 26(7), 1427-1432.

Thurai, M., Bringi, V.N. , Petersen, W.A., 2009. Rain microstructure retrievals using 2-D video disdrometer and C-band polarimetric radar. Adv. Geosci. 20, 13-18.

Thurai, M., Bringi, V.N., Petersen, W.A., Gatlin, P.N., 2013. Drop Shapes and Fall Speeds in Rain: Two Contrasting Examples. Journal of Applied Meteorology and Climatology 52(11), 2567-2581, doi: http://dx.doi.org/10.1175/JAMC-D-12-085.1

Verrier, S., Mallet, C., Barthès, L., 2011. Multiscaling properties of rain in the time domain, taking into account rain support biases . Journal of Geophysical Research: Atmospheres, 116(D20), D20119, http://dx.doi.org/10.1029/2011JD015719

Verrier, S., De Montera, L., Barthès, L., Mallet, C. , 2010. Multifractal analysis of African monsoon rain fields, taking into account the zero rain-rate problem . Journal of Hydrology 389 (1-2), 111-120.